

Third-Order Intermodulation in Microelectromechanical Filters Coupled With Capacitive Transducers

Ari T. Alastalo and Ville Kaajakari

Abstract—Third-order intermodulation in capacitively coupled microelectromechanical filters is analyzed. Parallel-plate transducers are assumed and, in addition to the capacitive nonlinearities, also the usually much weaker second- and third-order mechanical resonator nonlinearities are taken into account. Closed-form expressions for the output signal-to-interference ratio (SIR) and input intercept point are derived. The analytical results are verified in experiments and in numerical harmonic-balance simulations. It is shown that intermodulation as a function of frequency is asymmetric with respect to the passband. The results are valuable in designing micromechanical filters, for example, for communication applications. [1544]

Index Terms—Communication systems, intermodulation distortion, microelectromechanical devices.

I. INTRODUCTION

HIGH-QUALITY factor resonators are ubiquitous in today's communication devices. Macroscopic ceramic, SAW or FBAR filters offer excellent performance but their large size, high cost and unsuitability for IC integration limit their scope of application. In order to reduce the number of these bulky off-chip filters, receiver architectures such as direct conversion have been developed [1]. However, high-Q filters remain needed as band-select or channel-select filters to suppress interfering signals.

Miniature mechanical resonators, fabricated with microelectromechanical-systems (MEMS) technology, are a potential replacement of off-chip filters as they are compact in size and integratable with IC electronics [2]. The demonstrated quality factors of MEMS resonators, $Q > 100000$ at 10 MHz [3] and $Q > 1000$ at 1 GHz [4], are comparable to their macroscopic counterparts. While the mechanical properties of microresonators are very promising, obtaining a low electrical impedance ($\approx 50 \Omega$) is challenging, especially for the miniturized high frequency resonators that are mechanically stiff. To obtain low impedance levels, strong electromechanical transduction is needed which in case of electrostatic coupling requires a large bias voltage

and/or a narrow electrode gap. As large bias voltages are not preferred, narrow electrode gaps (< 200 nm) are often used, which introduces nonlinear electrostatic transducer forces and higher harmonics due to the inverse relationship between the electrode capacitance and the gap spacing. Additionally, mechanical nonlinear effects are possible in microresonators and fundamentally material nonlinearities set the limit for miniturization [5].

In filter applications, signal intermodulation (IM) due to odd-order nonlinearities is especially detrimental as it can lead to unwanted frequency components within the filter passband. For example, cubic mixing of two fundamental signals having frequencies ω_1 and ω_2 results in third-order intermodulation (IM3) products at frequencies $2\omega_1 - \omega_2$ and $2\omega_2 - \omega_1$. If $\omega_1 = \omega_0 + \Delta\omega$ and $\omega_2 = \omega_0 + 2\Delta\omega$, the IM product at $2\omega_1 - \omega_2$ is at the passband center frequency ω_0 corrupting the desired signal.

While complete linear models for the capacitively coupled resonators/filters have been developed [6], [7], intermodulation has received less attention. Navid *et al.* measured IM3 for a 10 MHz electrostatically coupled beam resonator [8]. They found that due to intermodulation distortion, there is a tradeoff between linearity and motional resistance. Their measured and calculated intermodulation results for interferers far below the passband were in agreement. However, since in [8] the analysis is based on transducer forces, not all mechanisms contributing to the intermodulation for varying interferer frequencies are taken into account. Our analysis is valid at both sides of the passband as well as for interferers within and close to the passband edge, where our results differ from those of [8]. Nolan *et al.* considered receivers with a linear MEMS filter preceding a nonlinear low-noise amplifier (LNA) [9]. They found that increasing the quality factor of the filter enhances the resulting signal-to-interference ratio (SIR). However, as we will show, this conclusion does not hold when the limiting intermodulation is due to nonlinearities of the MEMS filter.

In this paper, our prior analysis of in-band filter distortion [10] is extended to out-of-band interferers. Additionally, mechanical nonlinearities are included in the analysis. All intermodulation effects are taken into account to the first significant order and a closed form expression is derived for the signal-to-interference ratio (SIR). The analytical work is compared to numerical large-signal harmonic-balance simulations as well as to experiments and a good agreement is obtained. Due to the high motional impedance of micromechanical filters, classical filter matching to 50Ω seems challenging and the microfilters may

Manuscript received March 10, 2005; revised August 15, 2005. This work is supported by the Academy of Finland (grant 20542), Aplac[®] Solutions, VTI Technologies, Okmetic, and Tekes (National Technology Agency of Finland). Subject Editor K. Najafi.

The authors are with the VTT Technical Research Center of Finland, VTT Information Technology, Microsensing, Espoo, FIN-02044 VTT, Finland (e-mail: ari.alastalo@vtt.fi, ville.kaajakari@vtt.fi).

Digital Object Identifier 10.1109/JMEMS.2005.863705

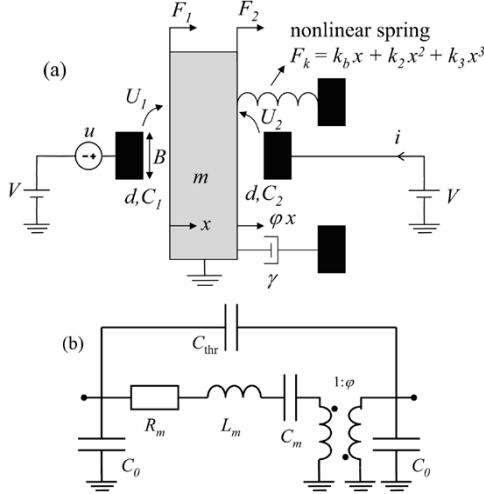


Fig. 1. (a) Capacitively coupled nonlinear resonator $\{k_b, k_2, k_3, m, \gamma\}$ filtering an electronic signal u . (b) Small-signal electrical equivalent model for the linear resonator with identical input and output transducers.

TABLE I
DEFINITIONS USED IN THE PAPER

C_0	$\epsilon_0 A/d$	ω_b	$\sqrt{k_b/m}$	\bar{i}	i/d
η	$C_0 V/d$	ω_0	$\sqrt{\bar{k}/m}$	α	$(\varphi - 1)/2$
k_e	$\eta V/d$	ω_e	$\sqrt{k_e/m}$	Γ	$\bar{u}_{\text{int},0}/\bar{u}_{\text{sig},0}$
\bar{k}	$k_b - 2k_e$	ω_1	$\omega_0 + \Delta\omega$	R_m	γ/η^2
\bar{k}_2	dk_2/k_e	ω_2	$\omega_0 + 2\Delta\omega$	C_m	η^2/\bar{k}
\bar{k}_3	$d^2 k_3/k_e$	\bar{u}	u/V (small)	L_m	m/η^2
Q	$\sqrt{\bar{k}m}/\gamma$	ξ	x/d (small)	q	$k_e Q/\bar{k}$

be best suited for on-chip channel select filtering where interfacing to 50Ω may not be required [2]. The analysis in this paper is therefore formulated in terms of filter input voltages and output currents to facilitate analysis with any source and load impedance with minimal effort.

The paper is organized as follows. First, in Section II, an analytical model for the intermodulation is developed. This is followed by Section III, where the analytical results are compared to measured and simulated intermodulation of two different microresonators. In Section IV, the present results are discussed and compared to other published results and the utility of the paper is demonstrated by calculating the IM for micromechanical filters at 1 GHz. Section V concludes the paper.

II. ANALYSIS

Fig. 1 shows a simplified model for a capacitively coupled mechanical resonator used as a filter and Table I collects the shorthand notations used in this paper. Here V is the bias

voltage, u is a small-signal input voltage and i is the output current. The zero-voltage gap of the input and output transducers is denoted d and x is the displacement of the resonating mass m . The linear and nonlinear mechanical spring constants of the resonator are k_b , k_2 and k_3 and γ is the damping coefficient. For generality, the displacement at the output transducer is related to the resonator displacement x by φx , where (1) is shown at the bottom of the page. In Section III, we will show measurement results for the both cases of (1). The capacitance values of the input and output transducers are

$$C_1 = \frac{\epsilon_0 A}{d + x} \quad (2a)$$

$$C_2 = \frac{\epsilon_0 A}{d - \varphi x} \quad (2b)$$

where A is the area of the transducer electrodes. The voltages across the transducers are $U_1 = V + u$ and $U_2 = V$ and the forces exerted by the transducers to the resonating mass are

$$F_i = \frac{1}{2} U_i^2 \frac{\partial C_i}{\partial x}, \quad i \in \{1, 2\}. \quad (3)$$

The positive direction of the force is as shown in Fig. 1.

The equation of motion for the resonator in Fig. 1 is

$$m\ddot{x} + \gamma\dot{x} + k_b x + k_2 x^2 + k_3 x^3 = F_1 + F_2 \quad (4)$$

where F_1 and F_2 are found from (3) after expanding the capacitances of (2a) and (2b) in power series as

$$C_1 = C_0 \left[1 - \left(\frac{x}{d}\right) + \left(\frac{x}{d}\right)^2 - \left(\frac{x}{d}\right)^3 + \dots \right] \quad (5a)$$

$$C_2 = C_0 \left[1 + \varphi \left(\frac{x}{d}\right) + \left(\frac{x}{d}\right)^2 + \varphi \left(\frac{x}{d}\right)^3 + \dots \right] \quad (5b)$$

where $C_0 \equiv \epsilon_0 A/d$. Taking nonlinearities into account up to third order in small parameters $\bar{u} \equiv u/V$ and $\xi \equiv x/d$, one finds for the equation of motion

$$\begin{aligned} \ddot{\xi} + \frac{\omega_0}{Q} \dot{\xi} + \omega_0^2 \xi = \omega_e^2 \left[\overset{(a)}{\alpha} - \overset{(b)}{\bar{u}} + (3\alpha - \overset{(c)}{\bar{k}_2}) \xi^2 + 2\bar{u}\xi - \frac{\overset{(d)}{\bar{u}^2}}{2} \right. \\ \left. + (4 - \overset{(f)}{\bar{k}_3}) \xi^3 - 3\bar{u}\xi^2 + \bar{u}^2 \xi \right] \\ \equiv F. \end{aligned} \quad (6)$$

For definitions of the variables in (6), see Table I. The time derivative is denoted with a dot. The fundamental frequency of the resonator is ω_0 . The dc force term (a) is nonzero for $\varphi = -1$ (1) which is the case for example for a BAW resonator in the square-extensional mode [3] or for a flexural-beam resonator if the input and output transducers are at the same side of the beam. For $\varphi = 1$ in (1), the dc force vanishes ($\alpha = 0$). For intermodulation performance, the dc term has no effect and will not be considered in what follows.

$$\varphi = \begin{cases} 1, & \text{e.g., for transducers at different sides of a flexural beam.} \\ -1, & \text{e.g., for transducers at the same side of a flexural beam or for a BAW resonator.} \end{cases} \quad (1)$$

For a force term $F(\omega)$ in the right-hand side of (6), the response function

$$H(\omega) = H'(\omega) + jH''(\omega) \equiv \left(\omega_0^2 - \omega^2 + j\frac{\omega\omega_0}{Q} \right)^{-1} \quad (7)$$

with real and imaginary parts

$$H'(\omega) = \frac{\omega_0^2 - \omega^2}{(\omega_0^2 - \omega^2)^2 + \left(\frac{\omega\omega_0}{Q}\right)^2}$$

$$H''(\omega) = \frac{-\frac{\omega\omega_0}{Q}}{(\omega_0^2 - \omega^2)^2 + \left(\frac{\omega\omega_0}{Q}\right)^2} \quad (8)$$

gives the linear solution as

$$\xi_{\text{lin}}(\omega) = FH' + \frac{\dot{F}H''}{\omega} \quad (9)$$

where the second term is due to dissipations. Note the short notation for the real and imaginary parts, H' and H'' , respectively. For the resonance frequency we have

$$H'(\omega_0) = 0$$

$$H''(\omega_0) = -\frac{Q}{\omega_0^2} \equiv H_0'' \quad (10)$$

The output current

$$i = \frac{\partial(C_2U_2)}{\partial t} = V\frac{\partial C_2}{\partial x}\dot{x} \quad (11)$$

can be expanded with (5b) as

$$\bar{i} \equiv \frac{i}{d} = \eta \left(\begin{array}{c} \varphi \\ \downarrow \\ \bar{i}_{\text{sig}}, \bar{i}_{\text{IM3}}^{(1)} \end{array} + 2\xi + 3\varphi\xi^2 + 4\xi^3 + \dots \right) \dot{\xi}. \quad (12)$$

Here we have indicated the terms that contribute to the signal and intermodulation currents at the fundamental frequency ω_0 . Since φ scales all the considered current terms and therefore does not affect SIR, φ is set to unity in the following analysis for simplicity.

Analytical expressions will now be derived for the signal current \bar{i}_{sig} as well as for the two IM3 terms $\bar{i}_{\text{IM3}}^{(1)}$ and $\bar{i}_{\text{IM3}}^{(2)}$ in (12) and the resulting SIR will be discussed. The desired signal \bar{u}_{sig} at the resonance frequency ω_0 and an interfering signal \bar{u}_{int} at the filter input are

$$\bar{u}_{\text{sig}} = \bar{u}_{\text{sig},0} \cos \omega_0 t \quad (13a)$$

$$\bar{u}_{\text{int}} = \bar{u}_{\text{int},0} (\cos \omega_1 t + \cos \omega_2 t) \quad (13b)$$

where

$$\omega_1 \equiv \omega_0 + \Delta\omega$$

$$\omega_2 \equiv \omega_0 + 2\Delta\omega. \quad (14)$$

The linear motion due to the excitations (13a) and (13b) is easily found with (6) (b), and (9)

$$\xi_{\text{sig}} = H_0'' \omega_e^2 \bar{u}_{\text{sig},0} \sin \omega_0 t \quad (15a)$$

$$\xi_{\text{int}} = -\omega_e^2 \bar{u}_{\text{int},0} \left(H_1' \cos \omega_1 t - H_1'' \sin \omega_1 t \right. \\ \left. + H_2' \cos \omega_2 t - H_2'' \sin \omega_2 t \right). \quad (15b)$$

Here $H_i \equiv H(\omega_i)$. The signal output current is with (12)

$$\bar{i}_{\text{sig}} = \eta \dot{\xi}_{\text{sig}} = \eta H_0'' \omega_e^2 \omega_0 \bar{u}_{\text{sig},0} \cos \omega_0 t \equiv \bar{i}_{\text{sig}}^I \cos \omega_0 t. \quad (16)$$

The signal current is in phase with the signal input voltage (13a) and its amplitude is denoted \bar{i}_{sig}^I .

To obtain a first-order estimate for the intermodulation current \bar{i}_{IM3} at ω_0 due to the interference motion at ω_1 and ω_2 (15b) requires some work. We assume that $\Delta\omega \ll \omega_0$ and that the Q value of the resonator is high enough to forbid motion at the harmonics of the excitation frequencies. Thus, the second-order terms (c,d,e) in (6) can be ignored. When the interference motion $\xi = \xi_{\text{int}}$ of (15b) and signal of (13b) are substituted to the third-order terms (f,g,h) in (6), a force $F_{\text{IM3}}(\omega_0)$ at $\omega_0 = 2\omega_1 - \omega_2$ is generated according to the formulas expressing trigonometric exponents and products, such as $\cos^2(\omega_1 t) \cos(\omega_2 t)$, in terms of first order functions, such as $\cos((2\omega_1 - \omega_2)t)$. The corresponding motion ξ_{IM3} at ω_0 , given by (9), results in an intermodulation current contribution $\bar{i}_{\text{IM3}}^{(1)}$ in (12)

$$\bar{i}_{\text{IM3}}^{(1)} = \eta \dot{\xi}_{\text{IM3}} \equiv \bar{i}_{\text{IM3}}^{I1} \cos \omega_0 t + \bar{i}_{\text{IM3}}^{Q1} \sin \omega_0 t, \quad (17)$$

where the subscripts I and Q refer to in-phase and quadrature components, respectively. The second contribution $\bar{i}_{\text{IM3}}^{(2)}$ to the intermodulation current is obtained by substituting $\xi = \xi_{\text{int}}$ of (15b) to the $3\eta\xi^2\dot{\xi}$ term in the current expansion (12) and is given by

$$\bar{i}_{\text{IM3}}^{(2)} = 3\eta\xi_{\text{int}}^2 \dot{\xi}_{\text{int}} \equiv \bar{i}_{\text{IM3}}^{I2} \cos \omega_0 t + \bar{i}_{\text{IM3}}^{Q2} \sin \omega_0 t. \quad (18)$$

The total intermodulation current is a sum of the two contributions (17) and (18)

$$\bar{i}_{\text{IM3}} = \bar{i}_{\text{IM3}}^{(1)} + \bar{i}_{\text{IM3}}^{(2)} \equiv \bar{i}_{\text{IM3}}^I \cos \omega_0 t + \bar{i}_{\text{IM3}}^Q \sin \omega_0 t \quad (19)$$

where

$$\bar{i}_{\text{IM3}}^I = \bar{i}_{\text{IM3}}^{I1} + \bar{i}_{\text{IM3}}^{I2} \quad (20a)$$

$$\bar{i}_{\text{IM3}}^Q = \bar{i}_{\text{IM3}}^{Q1} + \bar{i}_{\text{IM3}}^{Q2}. \quad (20b)$$

Thus, the two IM3 mechanisms, force intermodulation 1) and current intermodulation 2), can be summarized as:

- 1) & 2) Interfering signal: $\bar{u}_{\text{int}}(\omega_1, \omega_2)$
 $\xrightarrow{(6)(b)}$ interfering force: $F_{\text{int}}(\omega_1, \omega_2)$
 $\xrightarrow{(9)}$ linear displacement: $\xi_{\text{int}}(\omega_1, \omega_2)$

- 1) linear displacement $\xi_{\text{int}}(\omega_1, \omega_2)$
 $\xrightarrow{(6)(f,g,h)}$ IM3 force: $F_{\text{IM3}}(\omega_0)$
 $\xrightarrow{(9)}$ IM3 displacement: $\xi_{\text{IM3}}(\omega_0)$
 $\xrightarrow{(12)}$ IM3 current: $\bar{i}_{\text{IM3}}^{(1)}(\omega_0)$.

- 2) linear displacement $\xi_{\text{int}}(\omega_1, \omega_2)$
 $\xrightarrow{(12)}$ IM3 current $\bar{i}_{\text{IM3}}^{(2)}(\omega_0)$

The approximative nature of the analysis is mainly due to the IM3 displacement being only a first-order estimate of the solution to the nonlinear equation of motion (6).

After some algebra, the current contributions $\bar{i}_{\text{IM3}}^{\text{I1}}$, $\bar{i}_{\text{IM3}}^{\text{Q1}}$, $\bar{i}_{\text{IM3}}^{\text{I2}}$, and $\bar{i}_{\text{IM3}}^{\text{Q2}}$ in (17) and (18) can be written as

$$\bar{i}_{\text{IM3}}^{\text{I1}} = \frac{1}{4} \eta H_0'' \omega_e^4 \omega_0 \bar{u}_{\text{int},0}^3 \left\{ \begin{aligned} &2H_1' + H_2' \\ &+ 3 [H_1'^2 - H_1''^2 + 2H_1' H_2' + 2H_1'' H_2''] \omega_e^2 \\ &+ 3 [(H_1'^2 - H_1''^2) H_2' + 2H_1' H_1'' H_2''] \\ &\times (4 - \bar{k}_3) \omega_e^4 \end{aligned} \right\}, \quad (21a)$$

$$\bar{i}_{\text{IM3}}^{\text{Q1}} = -\frac{1}{4} \eta H_0'' \omega_e^4 \omega_0 \bar{u}_{\text{int},0}^3 \left\{ \begin{aligned} &2H_1'' - H_2'' + 6 [H_1' H_1'' + H_1'' H_2' - H_1' H_2''] \omega_e^2 \\ &+ 3 [(H_1''^2 - H_1'^2) H_2'' + 2H_1' H_1'' H_2''] \\ &\times (4 - \bar{k}_3) \omega_e^4 \end{aligned} \right\}, \quad (21b)$$

$$\bar{i}_{\text{IM3}}^{\text{I2}} = \frac{3}{4} \eta \omega_e^6 \omega_0 \bar{u}_{\text{int},0}^3 [(H_1''^2 - H_1'^2) H_2'' + 2H_1' H_1'' H_2''], \quad (21c)$$

$$\bar{i}_{\text{IM3}}^{\text{Q2}} = \frac{3}{4} \eta \omega_e^6 \omega_0 \bar{u}_{\text{int},0}^3 [(H_1'^2 - H_1''^2) H_2' + 2H_1' H_1'' H_2'']. \quad (21d)$$

Equations (21a) and (21c) give the amplitude of the in-phase intermodulation current $\bar{i}_{\text{IM3}}^{\text{I1}}$ (20a), while (21b) and (21d) give the quadrature-phase current $\bar{i}_{\text{IM3}}^{\text{Q1}}$ (20b). The signal-to-interference (or signal-to-intermodulation) ratio (SIR) can now be expressed as

$$\text{SIR} = \frac{\bar{i}_{\text{sig}}^{\text{I1}}}{\sqrt{(\bar{i}_{\text{IM3}}^{\text{I1}})^2 + (\bar{i}_{\text{IM3}}^{\text{Q1}})^2}}. \quad (22)$$

At the limit $Q \rightarrow \infty$, (22) is determined by the first in-phase current component $\bar{i}_{\text{IM3}}^{\text{I1}}$ of (21a) only. This is seen from the limits of the response functions as $Q \rightarrow \infty$: $H_0'' \rightarrow \infty$, $H_{i \neq 0}' \rightarrow 1/(\omega_0^2 - \omega_i^2) = \text{finite}$ and $H_{i \neq 0}'' \rightarrow 0$. Thus $\bar{i}_{\text{IM3}}^{\text{I1}}$ is the only nonlinear current component that goes to infinity in addition to the linear current $\bar{i}_{\text{sig}}^{\text{I1}}$ in (22) resulting in finite SIR. The quadrature currents in (21b) and (21d) approach a finite value while $\bar{i}_{\text{IM3}}^{\text{I2}}$ in (21c) vanish as $Q \rightarrow \infty$. Consequently, (22) simplifies considerably as shown by (23) at the bottom of the page where $\Gamma \equiv \bar{u}_{\text{int},0}/\bar{u}_{\text{sig},0}$ is the interference-to-signal ratio at the filter input. As will be illustrated with measurements in Section III, (22) can actually be approximated by (23) as soon as the interfering signals are outside the resonator passband. The labels (f), (g) and (h) in (23) correspond to those in (6) showing the origin

of different SIR contributions. As (23) contains odd powers of $\Delta\omega$, it is asymmetric around the resonance predicting different SIR values for interferers below the resonance and interferers above the resonance. Especially, the odd-order term labeled (g) in (23) proves to be important in Section III.

The third-order intercept point (IP3) is a useful measure of linearity and is typically defined as the crossing point of the linear extrapolations of the small-amplitude IM3 signal and a fundamental two-tone test signal in the device output. For frequency selective components such as filters, the above definition may be modified as IP3 being the crossing point of the linear extrapolations of the IM3 output signal and a wanted output signal when the wanted signal has the same input magnitude as the interferers and is located at the passband center. The signal level at the filter input, corresponding to IP3, is termed IIP3 and is found from SIR as [11]

$$\bar{u}_{0,\text{IIP3}}^2 = \frac{\text{SIR} \bar{u}_{\text{int},0}^3}{\bar{u}_{\text{sig},0}} = \text{SIR} \bar{u}_{\text{sig},0}^2 \Gamma^3. \quad (24)$$

Alternatively, IIP3 is obtained by setting $\Gamma = \bar{u}_{\text{int},0}/\bar{u}_{\text{sig},0} = 1$ in (22) or (23) and solving for the signal amplitude that gives SIR = 1.

The in-band result, given in [10], is obtained in the limit $\Delta\omega \rightarrow 0$ and $\bar{k}_3 \rightarrow 0$. With nonvanishing mechanical nonlinearities ($\bar{k}_3 \neq 0$), the result of [10] is slightly modified to

$$\bar{u}_{0,\text{IIP3},\Delta\omega=0}^2 = \frac{1}{\sqrt{\left[3 \left(\frac{1-\bar{k}_3}{4}\right) q^3 + \frac{q}{4}\right]^2 + \frac{9q^4}{4}}} \quad (25)$$

where

$$q \equiv \frac{k_e Q}{k} = \frac{Q \omega_e^2}{\omega_0^2} \approx \frac{Q}{\beta} \left(\frac{V}{U_{\text{pi}}}\right)^2. \quad (26)$$

Here the approximation is valid if $k_e \ll k \Leftrightarrow V \ll U_{\text{pi}}$ and the electromechanical pull-in voltage, at which bias level the resonator becomes unstable, is

$$U_{\text{pi}} = \sqrt{\frac{k_b d^2}{\beta C_0}} \quad (27)$$

where $\beta = 2$ for $\varphi = 1$ (bias forces act at opposite directions on the resonator) and $\beta = 27/8$ for $\varphi = -1$ in (1). As discussed in [10] the strongest contribution in (25) for high q is due to the ξ^3 nonlinearity in (6) (f). On the other hand, as the interferers are moved far outside the passband, the ξ^3 term becomes unimportant in SIR.

III. EXPERIMENTAL VERIFICATION

To verify the intermodulation model, narrow gap single-crystal silicon (SCS) resonators fabricated on silicon-on-insulator (SOI) wafers were characterized with linear and nonlinear

$$\text{SIR}_\infty = \frac{16|\Delta\omega|^3(\omega_0 + \Delta\omega)(2\omega_0 + \Delta\omega)^2}{\left[\begin{array}{c} 9\Delta\omega^4 \\ (h) \end{array} + 28\Delta\omega^3\omega_0 + 2\Delta\omega^2 \left(\begin{array}{c} 10\omega_0^2 - 9\omega_e^2 \\ (h) \quad (g) \end{array} \right) - 24\Delta\omega\omega_e^2\omega_0 + 3 \left(\begin{array}{c} 4 - \bar{k}_3 \\ (f) \end{array} \right) \omega_e^4 \right] \Gamma^3 \bar{u}_{\text{sig},0}^2 \omega_e^2} \quad (23)$$

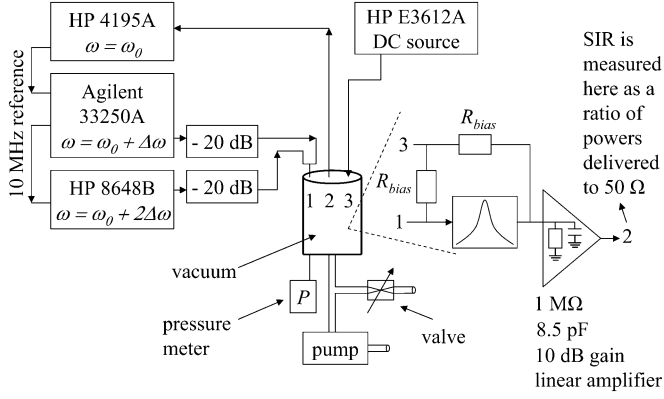


Fig. 2. Measurement setup. Pressure (P) in the vacuum chamber is measured and controlled using the valve to vary the Q value of the resonator.

excitation. As the fabrication process is detailed elsewhere [12], only the experimental setup and results are given here.

A. Measurement Setup

Fig. 2 shows the measurement setup used to validate the analytical results. The resonator is kept in a vacuum chamber together with a JFET preamplifier that has a gain of 10 dB, an input resistance of 1 M Ω , and an input capacitance of 8.5 pF. Pressure in the chamber is controlled with a valve to tune the Q value of the resonator. To measure the intermodulation at ω_0 , signals at $\omega_0 + \Delta\omega$ and $\omega_0 + 2\Delta\omega$ are generated and summed at the resonator input. The signal generators (Agilent 33250A and HP 8648B) are isolated with 20 dB attenuators to prevent intermodulation at the signal sources. The resonator output signal is buffered with a preamplifier and measured with a spectrum analyzer (HP 4195A). As the preamplifier is kept in its linear range, it does not affect the SIR. The signal generators and the spectrum analyzer are locked to a common frequency reference. The desired-signal output power is measured with one of the signal generators turned off and the other tuned to ω_0 .

B. Simulation Model

To accurately model the characterized microresonators, the resonator, the electric biasing, and read-out circuitry are implemented in a circuit simulator [14]. The resonator is modeled as an electrical equivalent of the spring-mass system in Fig. 1. For the capacitive coupling, the accurate nonlinear model is used [13]. The simulations are used: i) to obtain good estimates of the mechanical and electrical parameters by fitting the simulated transmission curves to the measured responses and ii) to verify the analytical model of the intermodulation. For the intermodulation simulations, the large-signal harmonic-balance analysis with multiple input and output signal tones is used. As the harmonic-balance analysis is carried out in the frequency domain, it is computationally efficient for systems that have high quality factors and are thus slow to settle in the time-domain (transient) analysis [15]. Schematic of the simulation setup is shown in Fig. 3.

C. BAW Resonator

Fig. 4(a) shows the schematic of a bulk-acoustic-wave (BAW) resonator oscillating in the square-extensional mode [3]

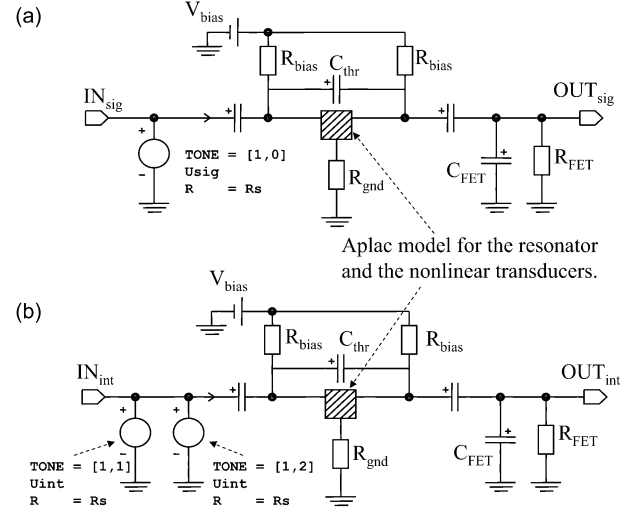


Fig. 3. Schematic of the harmonic-balance Aplac[®]-circuit-simulator model [13] for the desired signal (a) and the interferers (b). The model for the resonator (see Fig. 1) and the nonlinear transducers are included in the shaded three-port components. SIR is determined as the ratio of OUT_{sig} voltage to OUT_{int} voltage at the fundamental frequency.

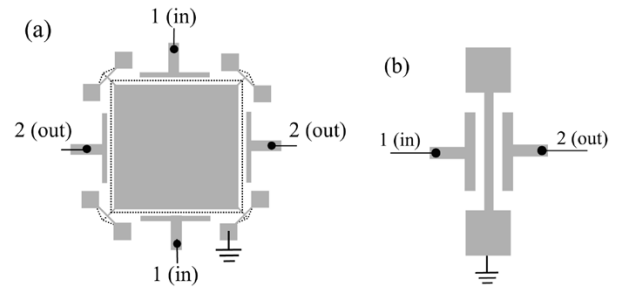
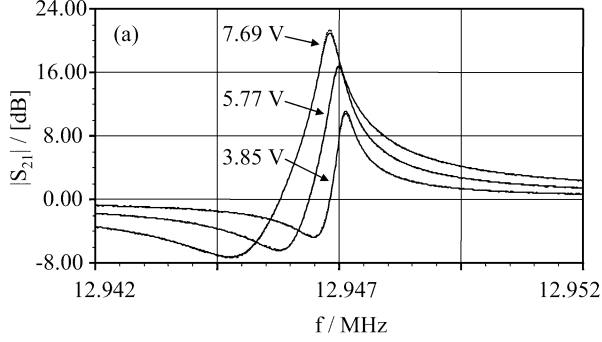
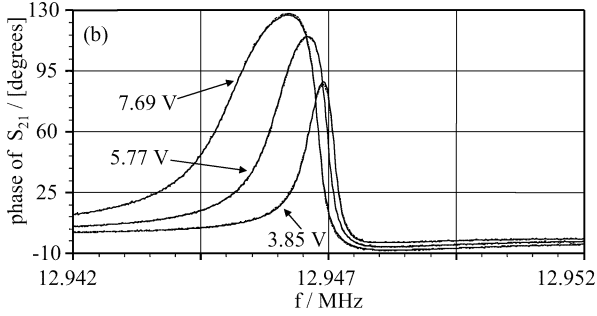


Fig. 4. Schematics of the two experimentally characterized resonators. Also indicated are the input and output ports corresponding to 1 and 2 in Fig. 2. (a) BAW resonator in the square-extensional mode [3]. The dotted lines illustrate the movement of the plate from the rest position. The two input ports as well as the two output ports are electrically shorted. (b) Clamped-clamped flexural beam resonator [10].

for which $\varphi = -1$ in (1) (all the faces of the square plate move in phase). The resonator is fabricated on a silicon-on-insulator (SOI) wafer and has a size of 320 $\mu\text{m} \times 320 \mu\text{m} \times 10 \mu\text{m}$. Two transducers at opposite sides of the square plate are used for signal input and output. Fitting the simulated response to measured behavior at different bias voltages, as shown in Fig. 5, allows one to find the equivalent-model parameters given in Table II. Fitting was done by adjusting the spring constant k_b , eigenfrequency ω_b , Q value, feed-through capacitance C_{thr} , gap d , and R_{gnd} that is a parasitic contact resistance at the ground connect of the resonator and accounts for the weakening of the antiresonance in Fig. 5(a). The same order of DC resistance for R_{gnd} was also measured. As the capacitive nonlinearity is the dominant effect, the mechanical nonlinearities k_2 and k_3 are neglected (for the 184 nm gap, the capacitive nonlinearity dominates at bias voltages greater than 2.5 V) [5]. With a 5.77 V bias voltage, corresponding to the middle curve in Fig. 5, the theoretical estimate of in-band IIP3 given by (22) is 21 dBm (corresponding to a 50 Ω source impedance) and the estimate for off-resonance interferers with $\Delta f = 1$ kHz, given by (23) and (24), is IIP3 = 38 dBm.



(a) Amplitude of S_{21} . The antiresonance is weakened due to nonzero resistance in the ground connect of the resonator.



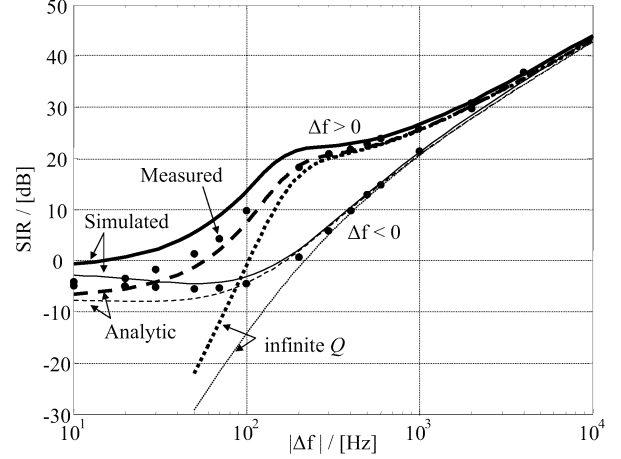
(b) Phase of S_{21} .

Fig. 5. Measured (dashed lines) and simulated (solid lines) S_{21} for the BAW resonator with three different bias voltages. The result is calibrated with a zero-bias response, that is, S_{21} is defined as the ratio of the motional current through the electrical-equivalent RLC circuit of Fig. 1 to the parasitic feed-through current through C_{thr} . Measured and simulated results differ slightly only at the peaks of the curves.

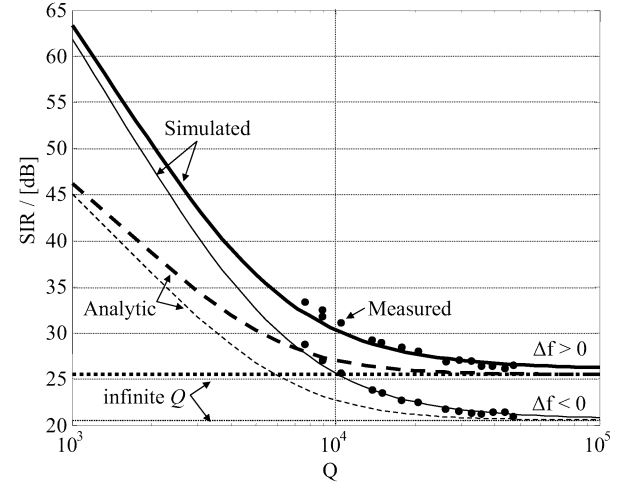
TABLE II
PARAMETER VALUES FOR THE BAW RESONATOR. VALUES AT THE BOTTOM ROW ARE FOR 5.77 V BIAS VOLTAGE

k_b	16.3 MN/m	f_b	12.947 MHz	U_{pi}	730 V
d	184 nm	Q	46900	k_e	300 N/m
C_0	307 fF	C_{thr}	35.4 fF	R_{gnd}	1.2 k Ω
R_m	46.2 k Ω	L_m	26.6 H	C_m	5.67 aF

Fig. 6(a) shows the measured, simulated and analytic results, all in very good agreement, for the SIR as a function of interferer separation at the output of the BAW resonator with the signal (13a) and interferer (13b) input powers of $P_{sig} = -50$ dBm and $P_{int} = 0$ dBm, respectively. The large interferer power was chosen to obtain a sufficient signal-to-noise ratio in the measurements. The infinite- Q limit of (23) becomes valid as soon as the interferers are outside the resonator passband of $\Delta f_{3dB} = f_0/Q \approx 300$ Hz for $Q = 46900$ in vacuum. Also, as predicted from the theory, at intermediate frequencies of $50 \text{ Hz} < |\Delta f| < 1 \text{ kHz}$ we observe that the SIR is much lower for interferers below the resonance ($\Delta f < 0$) than for interferers above the resonance ($\Delta f > 0$). The difference between the SIR for $\Delta f > 0$ and $\Delta f < 0$ is at greatest when the interferer frequencies are close to the 3-dB-passband edge of the resonator. Of the odd-order $\Delta\omega$ terms in (23) that explain this difference, the one originating from (g) in (6) dominates.



(a) Signal-to-intermodulation ratio with $Q = 46900$ as a function of interferer frequency separation Δf .



(b) Signal-to-intermodulation ratio as a function of resonator Q value with $|\Delta f| = 1 \text{ kHz}$.

Fig. 6. Simulated (solid), analytic (22) (dashed), analytic for $Q \rightarrow \infty$ (23) (dotted) and measured (large dots) intermodulation results for the BAW resonator are shown for $\Delta f < 0$ (thin lines) and $\Delta f > 0$ (thick lines). Bias voltage is 5.77 V corresponding to the middle curve in Fig. 5. The signal and interferer input powers are $P_{sig} = -50$ dBm and $P_{int} = 0$ dBm.

Fig. 6(b) shows the SIR at constant interferer separation for different quality factors obtained by adjusting the chamber pressure. At low Q , the analytic estimates expectedly deviate from the measured and simulated results due to the approximations utilized in Section II. Increasing Q reduces SIR toward the infinite- Q limit (23).

Fig. 7 shows the different intermodulation current components \bar{i}_{IM3}^{Q1} , \bar{i}_{IM3}^{Q1} , \bar{i}_{IM3}^{Q2} , and \bar{i}_{IM3}^{Q2} in (21a)–(21d) as functions of the interferer frequency separation. It is seen that the force intermodulation mechanism 1) dominates over the current intermodulation 2), that is, $|\bar{i}_{IM3}^{Q1}| \geq |\bar{i}_{IM3}^{Q2}|$ and $|\bar{i}_{IM3}^{Q1}| \geq |\bar{i}_{IM3}^{Q2}|$ except at small positive Δf for which $|\bar{i}_{IM3}^{Q1}| < |\bar{i}_{IM3}^{Q2}|$.

D. Flexural Beam Resonator

To have a further justification of the analysis of Section II, we consider a flexural-beam resonator [10], shown schematically in Fig. 4(b), with $P_{sig} = -50$ dBm, $P_{int} = -10$ dBm and

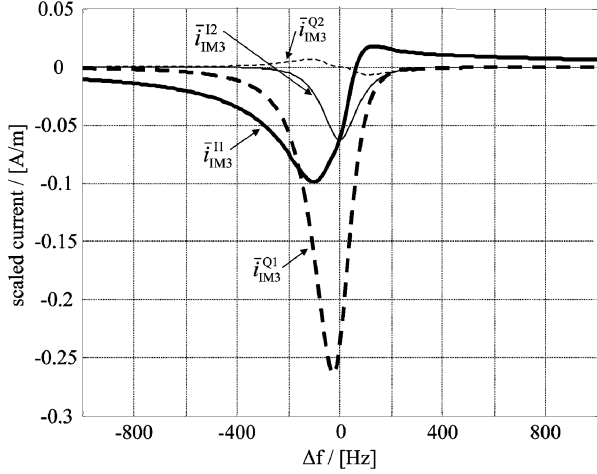


Fig. 7. Intermodulation current contributions (21a)–(21d) for the BAW resonator.

TABLE III
PARAMETERS FOR THE FLEXURAL-BEAM RESONATOR WITH A 13 V BIAS

k_b	8.3 kN/m	f_b	8.452 MHz	U_{pi}	102 V
d	188 nm	Q	1803	k_e	66 N/m
R_m	92.6 k Ω	L_m	3.14 H	C_m	115 aF

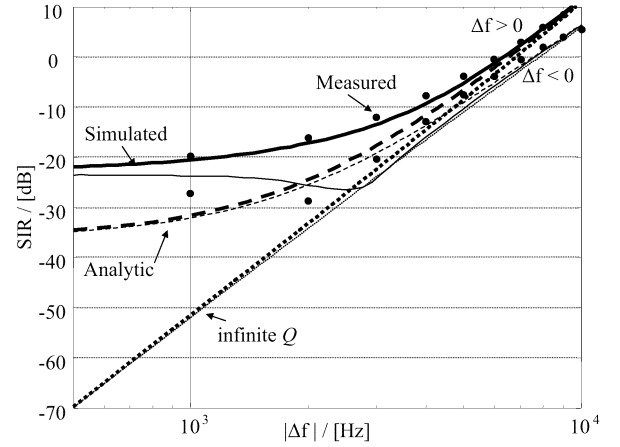
$V = 13$ V. Equivalent-model parameters for the beam resonator are given in Table III.

Fig. 8(a) shows the measured, simulated and analytic results for the SIR as a function of interferer separation. Again, a very good agreement is obtained and the predicted asymmetry in Δf is observed. At small Δf , the analytic result deviates from the measured and simulated. This is because the interferer power is of the same order as the in-band IIP3 point [10] and thus the intermodulation signal at ω_0 is weaker than its analytical estimate. Fig. 8(b) shows the SIR at different quality factors. Here the Q value is considerably lower than for the BAW resonator and as much tuning range is not obtained by varying the pressure in the vacuum chamber.

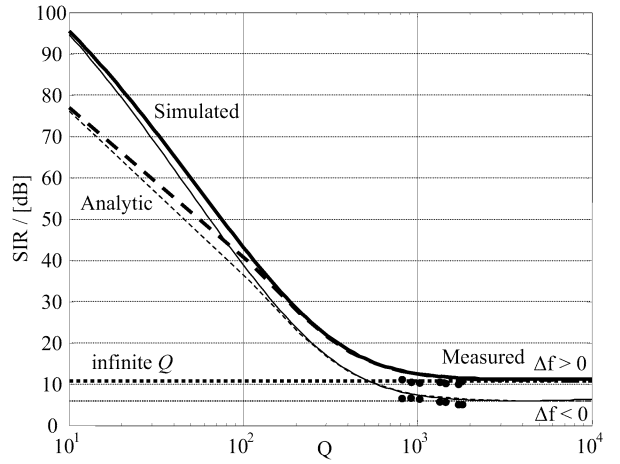
IV. DISCUSSION

In this paper, a concise formulation for SIR and IIP3 in capacitively coupled micromechanical filters is given. The experimental verification is provided for two single-resonator structures but the formulation applies to all single-stage MEMS filters that are coupled with parallel-plate transducers. Such filters could be used to construct a receiver front-end structure having a bank of narrow-band (ultimately channel-select) filters with different passbands to cover all the RX channels [2]. While the results in the present paper are believed to be indicative of the MEMS filter performance in general, further work is needed to expand the analytical results to more complex multi-stage filter structures. This will be a subject of future research.

In the paper, the motional impedances are much higher (> 40 k Ω) than the source and load impedances (see Figs. 1 and 2). As the analysis has been formulated in terms of input voltages and output currents, the derived expressions for SIR and IIP3 are valid also for tightly coupled resonators with source and load impedances being comparable to or larger than the



(a) Signal-to-intermodulation ratio with $Q = 1803$ as a function of interferer frequency separation Δf .



(b) Signal-to-intermodulation ratio as a function of resonator Q value with $|\Delta f| = 10$ kHz.

Fig. 8. As Fig. 6 (thick lines for $\Delta f > 0$ and thin lines for $\Delta f < 0$) but for the flexural-beam resonator [10]. Bias voltage is 13 V, $P_{sig} = -50$ dBm, and $P_{int} = -10$ dBm.

motional impedance provided that: i) the source and filter input impedances are used to adjust the resonator input voltages and ii) the loaded in-circuit quality factor is used for SIR calculations. What is not taken into account is that in the strongly coupled case, the motional impedance is a strong function of frequency and the different interfering signals now see different mechanical impedances. Consequently, the interference input voltage levels do not remain equal as assumed in this paper. However, simulations show that this effect is not significant. Finally, we note that for strong interferers within the passband, Duffing effect results in signal compression that may also limit the filter performance [5].

The previously obtained experimental IM3 results of [8] for $\Delta f \ll -f_0/Q$ are in good agreement with (23). For example, assuming that the spring constant of the beam can be approximated by the point-force result $k_b = 16YH(w/L)^3$ [16], where Y is the Young modulus, (23) and (24) give the same IIP3 voltage of $V_{IIP3} \equiv u_{0,IIP3} = 68$ dBmV (corresponding to 18 dBm with a 50 Ω source impedance) as reported in Fig. 5 of [8]. On the other hand, for $\Delta f > 0$ as well as for the interferers close to the passband edge, our results (22)–(24) differ from the analytical results (absolute value of (11)) in [8] by up to 10 dB for the BAW and flexural-beam examples of this paper.

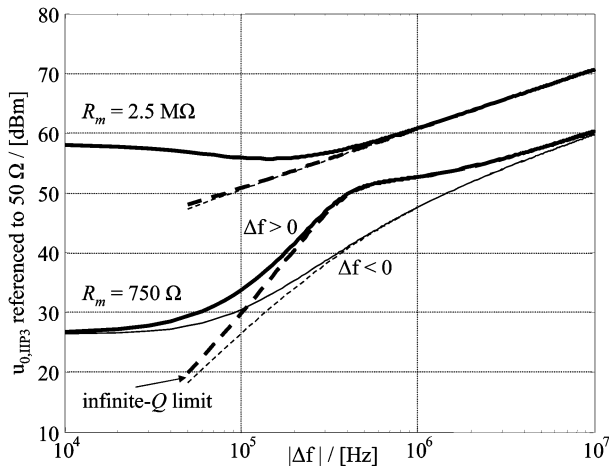


Fig. 9. The theoretical IIP3 voltage from (22)–(24) for the 1.156 GHz resonators of [4]. The curves for $R_m = 2.5 \text{ M}\Omega$ are for a fabricated device while $R_m = 750 \text{ }\Omega$ corresponds to a theoretical device.

To further demonstrate the utility of this paper, we consider the recently reported radial-mode 1.156 GHz disk resonators of [4]. Fig. 9 shows the IIP3 voltage, corresponding to a $50 \text{ }\Omega$ source impedance, given by (22)–(24) for a measured and a theoretical improved resonator. For the fabricated device with a motional resistance of $R_m = 2.5 \text{ M}\Omega$, the SIR is symmetric around the passband. The exceptionally high IIP3 is not surprising as most of the power is reflected due to impedance mismatch. For the theoretical device with $R_m = 750 \text{ }\Omega$ that has an improved electromechanical coupling and correspondingly better impedance match and lower IIP3, there is a clear asymmetry of IIP3 with respect to Δf also outside the passband of $\Delta f_{3\text{dB}} = f_0/Q \approx 200 \text{ kHz}$. Both resonators of Fig. 9 have an IIP3 that meet the requirements set, for example, for GSM receivers [17]. On the other hand, the motional resistance is still far from $50 \text{ }\Omega$ even for the theoretical device. Lower resistances can be obtained, for example, by reducing the gap and/or increasing the bias voltage which, however, lowers the IIP3 [8].

V. CONCLUSION

Detailed analysis of intermodulation in capacitively coupled MEMS filters was presented and closed form expressions for SIR and IIP3 were derived. It was shown that the force intermodulation mechanism is usually the dominant effect. However, close to or within the filter passband, the current intermodulation mechanism is also important. The analytical results were verified with experiments and simulations and excellent agreement was obtained.

The results of this paper may be used in designing micromechanical filters, for example, for communication applications. Well outside the passband, the obtained SIR does not depend on the quality factor. Within the passband, increasing the quality factor lowers the IIP3. The asymmetry observed near the passband edge results in interferers below the passband being more difficult to block than interferers above the passband.

ACKNOWLEDGMENT

The authors would like to thank J. Kiihamäki for fabricating the microresonators used in the measurements and J. Holmberg for useful discussions concerning the measurements.

REFERENCES

- [1] T. Lee, *The Design of CMOS Radio-Frequency Integrated Circuits*. Cambridge, U.K.: Cambridge University Press, 1998.
- [2] C. T.-C. Nguyen, "Frequency-selective mems for miniaturized low-power communication devices," *IEEE Trans. Microw. Theory Tech.*, vol. 47, pp. 1486–1503, Aug. 1999.
- [3] V. Kaajakari, T. Mattila, A. Oja, J. Kiihamäki, and H. Seppä, "Square-extensional mode single-crystal silicon micromechanical resonator for low phase noise oscillator applications," *IEEE Electron Device Lett.*, vol. 25, pp. 173–175, Apr. 2004.
- [4] J. Wang, Z. Ren, and C. T.-C. Nguyen, "1.156-GHz self-aligned vibrating micromechanical disk resonator," *IEEE Trans. Ultrason., Ferroelect., Freq. Contr.*, vol. 51, pp. 1607–1628, Dec. 2004.
- [5] V. Kaajakari, T. Mattila, A. Oja, and H. Seppä, "Nonlinear limits for single-crystal silicon microresonators," *J. Microelectromech. Syst.*, vol. 13, pp. 715–724, Oct. 2004.
- [6] H. Tilmans, "Equivalent circuit representation of electromechanical transducers: I. Lumped-parameter systems," *J. Micromech. Microeng.*, vol. 6, no. 1, pp. 157–176, Mar. 1996.
- [7] L. Lin, R. T. Howe, and A. P. Pisano, "Microelectromechanical filters for signal processing," *J. Microelectromech. Syst.*, vol. 7, pp. 286–294, Sep. 1998.
- [8] R. Navid, J. R. Clark, M. Demirci, and C. T. C. Nguyen, *Proc. Third-Order Intermodulation Distortion in Capacitively-Driven Cc-Beam Micromechanical Resonators*, Interlaken, Switzerland, 2001, pp. 228–231.
- [9] T. C. Nolan and W. E. Stark, "Mitigation of cosite interference in nonlinear receivers with mems filters," in *Proc. MILCOM 2000. 21st Century Military Communications Conference*, Oct. 2000, pp. 769–773.
- [10] A. T. Alastalo and V. Kaajakari, "Intermodulation in capacitively coupled microelectromechanical filters," *IEEE Electron Device Lett.*, vol. 26, pp. 289–291, May 2005.
- [11] B. Razavi, *RF Microelectronics*: Prentice Hall, 1998.
- [12] J. Kiihamäki, V. Kaajakari, H. Luoto, H. Kattelus, and M. Ylikoski, "Fabrication of single crystal silicon resonators with narrow gaps," in *Proc. Transducers'05, The 13th International Conference on Solid-State Sensors, Actuators and Microsystems*, Seoul, Korea, Jun. 5–9, 2005, pp. 1354–1357.
- [13] T. Veijola and T. Mattila, "Modeling of nonlinear micromechanical resonators and their simulation with the harmonic-balance method," *International Journal of RF and Microwave Computer Aided Engineering*, vol. 11, no. 5, pp. 310–321, Sep. 2001.
- [14] Aplac RF Design Tool. APLAC Solutions Corp.. [Online]. Available: www.aplac.com
- [15] S. Maas, *Nonlinear Microwave and RF Circuits*, 2nd ed. Norwood, MA: Artech House, 2003.
- [16] J. W. Weaver, S. Timoshenko, and D. Young, *Vibration Problems in Engineering*, 5th ed. New York, NY: Wiley, 1990.
- [17] "GSM Global System for Mobile Communications," ETSI, 3GPP ts 05.01/05.05, 2003.



Ari T. Alastalo received the M.Sc. degree in technical physics from Helsinki University of Technology (HUT), Finland, in 1997.

From 1996 to 1998 he was an assistant at HUT working in the area of magnetic quantum impurities. From 1998 to 2001, he was with Nokia Research Center carrying out research of radio propagation, RF architectures, baseband algorithms, and protocols for adaptive-antenna systems. Since 2002, he has been a Research Scientist at VTT Information Technology, Finland. His present research focuses on RF MEMS.



Ville Kaajakari received the M.S. and Ph.D. degrees in electrical and computer engineering from University of Wisconsin-Madison in 2001 and 2002, respectively.

He is currently Senior Research Scientist at VTT Information Technology, Finland, where his research interest is RF-MEMS.